

Large-eddy Simulation of Flow Separation Control by Spanwise Alternatively Distributed Strips Control

W. Ni**, L. Lu*, J. Fang**, C. Moulinec**, D. R. Emerson** and Y. Yao***

Corresponding author: jian.fang@stfc.ac.uk

* National Key Laboratory of Science and Technology on Aero-Engine Aero-Thermodynamics, School of Energy and Power Engineering, Beihang University, Beijing, 100191, China

** Scientific Computing Department, Science & Technology Facilities Council (STFC) Daresbury Laboratory, Warrington, WA4 4AD, UK

*** Faculty of Environment and Technology, Department of Engineering Design and Mathematics, University of the West of England, Bristol, BS16 1QY, UK

Abstract: An implicit large-eddy simulation (ILES) study is presented for turbulent boundary layer separation from a backward-facing rounded ramp with active wall actuations control. This method, namely spanwise alternatively distributed strips (SADS) control, is imposed onto the flat plate surface upstream of the ramp by alternatively applying out-of-phase control (OPC) and in-phase control (IPC) to the wall-normal velocity component in the lateral direction. As a result, the local turbulence is alternatively suppressed by OPC strips and enhanced by IPC strips, leading to the creation of a vertical shear layer, which is responsible for the generation of the large-scale streamwise vortices (LSSVs). These LSSVs, thought to be similar to Prandtl's second kind of secondary flow, can be further sustained by the SADS control, exerting a predominant influence on the suppression of the flow separation. The interaction among the LSSV, the downstream recirculation zone and free-shear layer is studied by examining flow statistics, including skin-friction, wall pressure coefficients, skin friction lines, mean streamwise velocity, turbulent kinetic energy and Reynolds stress. It is found that the flow separation is delayed by the SADS control and the size of the mean recirculation zone is reduced.

Keywords: Implicit large-eddy simulation (ILES), Backward-Facing Rounded Ramp, Spanwise Alternatively Distributed Strips (SADS) Control, Turbulent Secondary Flow, Flow Separation

1 Introduction

Flow separation control, historically considered as boundary layer control, is probably the oldest and most crucial in economic sense, among all the existing flow control methods [1], since boundary layer separation has many negative influences on the performance of vehicles and devices, including drag increase, flow blockage and instability. As an effective strategy of suppressing flow separation, significant effort has been devoted to vortex generators (VGs) for decades [2]-[4]. The large-scale streamwise vortices (LSSVs) generated by VGs, which can enhance the momentum transport across the boundary layer, is believed to be crucial in suppressing separation. Although this concept works well, certain technical difficulties in practical applications, such as design integration and manufacturing, need to be dealt with because of local shape change. Recently, researchers have found that the large-scale motions can also be produced by small-scale wall disturbance, for example, using

riblets [5] or wall roughness [6]. As Vanderwel *et al.* [7] suggested, the generated large-scale motions have such a profound impact on the structure of the boundary layer and are readily accessible by altering the surface topography, these flows would have great potential for near-wall mixing and flow separation control. In the present research, based on our preliminary investigation in the channel flow [8],[9], the spanwise alternatively distributed strips (SADS) control, composed of alternatively imposed out-of-phase control (OPC) and in-phase control (IPC) wall-normal velocity actuations, is applied to a flow past a backward-facing ramp to study its effects in suppressing flow separation.

2 Methodology

The three-dimensional (3-D) unsteady compressible Navier-Stokes (N-S) equations in a general, time-invariant system are solved numerically. The N-S equations are non-dimensionalised with the reference density ρ_{ref} , the reference velocity u_{ref} , the temperature at wall T_{ref} and dynamic viscosity μ_{ref} as well as the height of the ramp H . The resulting dimensionless parameters are the Reynolds number $Re = \rho_{ref}u_{ref}H/\mu_{ref}$ and the Mach number $M = u_{ref}/\sqrt{\gamma RT_{ref}}$, set as 7,106 and 0.2 respectively. A constant Prandtl number $Pr = 0.72$ is used. The computational geometry under consideration is the same as that of Lardeau *et al.* [10],[11], as illustrated in Figure 1. The size of the computational domain is $55 \times (9-10) \times 5$, discretised with a mesh of $1290 \times 200 \times 300$. The ASTR code, which has been previously used in DNS/LES of turbulent flows [12]-[15], is adopted here to solve the N-S equations within the framework of high-order finite-difference method. The sixth-order compact central scheme [16] is adopted to calculate both the convective and diffusive terms. The tenth-order compact filter [17] is used to remove numerical wiggles at high wavenumbers. The filter also provides extra dissipation at subgrid scales and acts as a subgrid-scale models. Therefore, it defines an implicit large-eddy simulation (ILES), which was first introduced by Visbal *et al.* [17]-[20]. The topography configuration with equal spanwise width of OPC and IPC strips, namely Case WE, is presented in Figure 2a. As illustrated in Figure 2b, the active wall-normal velocities imposed by OPC and IPC are respectively given by $v_w(x, z) = -A_{OPC}v(x, y_{dtc}, z)$ and $v_w(x, z) = +A_{IPC}v(x, y_{dtc}, z)$ in the fully developed turbulent boundary layer upstream of the ramp from $x_{start} = -10.0$ to $x_{end} = 0.0$. $v_w(x, z)$ is the wall-normal velocity and y_{dtc} is the detected position taking as a fixed value of y coordinate at the 15th mesh node away from wall. The corresponding non-dimensional value y_{dtc}^+ ranges from 12 ($x = x_{start}$) to 15 ($x = x_{end}$), based on the wall values of the baseline case. The coefficients A_{OPC} and A_{IPC} are two parameters controlling the amplitude of the wall velocities, which are both set to 0.5 in the present study to improve the stability of the computation. The other two velocity components at the wall are kept to zero. A non-controlled flow past a backward-facing ramp (Case NC) is carried out first as the baseline case.

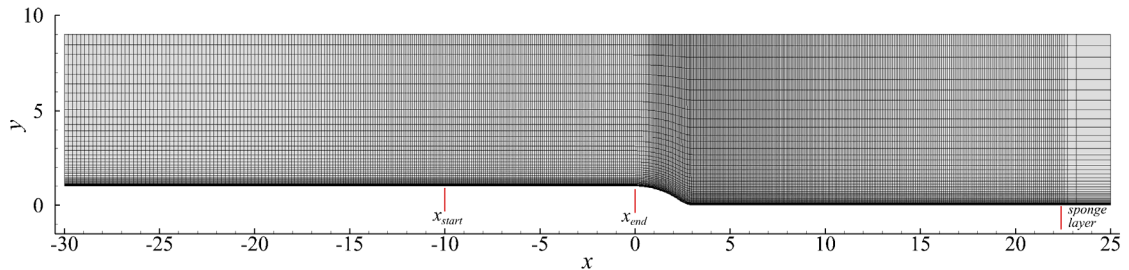


Figure 1: The sketch of the computation domain and reduced numerical mesh. The mesh is plotted every 5th grid lines in both x and y directions.

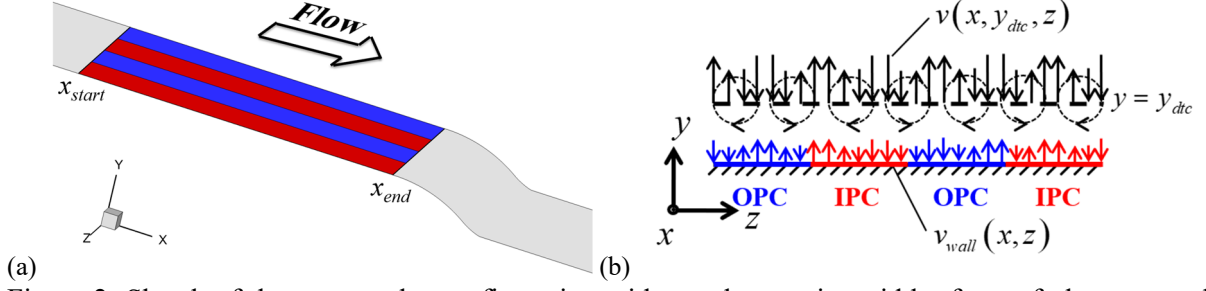


Figure 2: Sketch of the topography configuration with equal spanwise width of out-of-phase control (OPC, blue) and in-phase control (IPC, red) strips (a) and control method (b) used in the present study. The black and colored arrows represent the wall-normal velocity at the detected position and the wall respectively in (b).

3 Results and Discussion

3.1 Validation

The mean velocity profile $\langle \bar{u} \rangle_z$ of baseline case in the equilibrium zone is compared with the classic law of wall and the incompressible DNS data at $Re_\tau \approx 1000$ of Schlatter and Örlü [21] in Figure 3a. A good agreement in both the linear sub-layer and log-law layer is obtained and the difference in the wake layer is attributed to the Reynolds number effects [22]. In the present paper, "—" stands for the time-averaging operator and $\langle \cdot \rangle$ for the space-averaging operator, i.e. $\langle \cdot \rangle_z$ is used for the spanwise averaged variables. The fluctuations from each averaging operator are defined as $g' = g - \bar{g}$ and $g_{(z)} = g - \langle g \rangle_z$. The averaging operators can also be combined since they are all linear operators, i.e. $\langle \bar{g} \rangle_z$ and $g'_{(z)}$ might be used, for instance.

The root mean square (RMS) velocity fluctuations $u'_{i,rms} = \sqrt{\langle u'_{i,(z)} u'_{i,(z)} \rangle_z}$ ($i=1, 2, 3$) and Reynolds shear stress in the equilibrium zone of Case NC are compared with the DNS data of Schlatter and Örlü [21] and Jeménez *et al.* [23] in Figure 3b. A general good agreement for RMS velocity fluctuations and Reynolds shear stress is achieved.

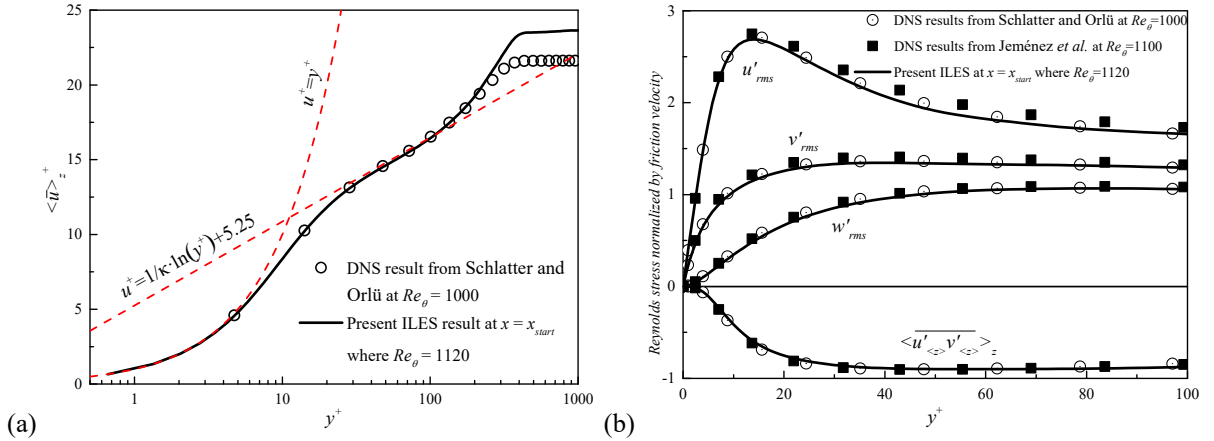


Figure 3: Mean velocity profile (a) and Reynolds stresses (b) in inner scaling. The von Kármán constant is $\kappa=0.41$.

3.2 Turbulent Structures

The turbulent coherent structures identified by the iso-surface of Q criterion [24] and colored with instantaneous streamwise vorticity ω_x of the two cases are presented in Figure 4. Compared with the baseline case, the turbulent coherent structures of Case WE are alternatively redistributed over the controlled region. In general, the turbulent coherent structures are enhanced above the IPC strips, whereas above the OPC strips, the suppressed coherent structures can be observed. The flow field

above the controlled zone demonstrates a phase-locked reorganization in corresponding to the topography configuration. The alternatively altered coherent structures above OPC/IPC strips exhibit the same tendency with those in the turbulent channel flows controlled by SADS [8][9], indicating the evidence of suppression/enhancement of the turbulence. Furthermore, the alternatively distributed suppressed and enhanced turbulent coherent structures can extend to the downstream of the controlled area even beyond the separation of the boundary layer as illustrated in Figure 4b. More quantitative detailed analysis of the case will be shown in the next subsection.

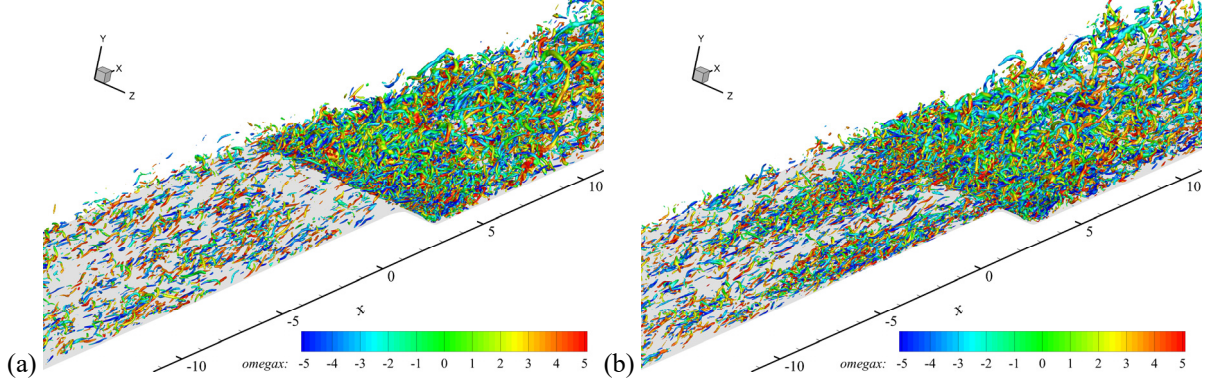


Figure 4: Turbulent coherent structures visualised by Q -criterion iso-surfaces and coloured by the instantaneous streamwise vorticity ω_x . (a) Case NC; (b) Case WE.

3.3 Mean Flow

3.3.1 Skin Friction and Pressure Coefficient

The streamwise variation of skin friction coefficient and pressure coefficient are firstly analyzed based on spanwise- and time-averaging statistics. The mean skin friction coefficient C_f and pressure coefficient C_p is defined as, respectively

$$C_f(x) = \frac{\mu_w \partial \langle \bar{u} \rangle_z / \partial y|_w}{\frac{1}{2} \rho_\infty u_\infty^2}, \quad (1)$$

and

$$C_p(x) = \frac{\langle \bar{P} \rangle_z - P_\infty}{\frac{1}{2} \rho_\infty u_\infty^2}. \quad (2)$$

It can be seen from Figure 5a that the near-wall flow upstream of the ramp undergoes the motion of acceleration and thus the skin friction coefficient rises to a relatively high level. It is due to the pressure drop induced by the convex curvature further downstream and the elliptic feature of the pressure field [11] as shown in Figure 5b. For Case WE, the skin frictions upstream of the ramp is distinctly increased by SADS, due to the intense activation on turbulence locally imposed by the IPC strips.

For the Case NC, the time-averaged separation occurs at $x=0.79$ and the flow reattaches at $x=5.03$. With the SADS control, the separation location is postponed to $x=0.92$ while the flow recovers from the recirculated state to the attached flow at $x=4.83$. Therefore, the size of the separation zone is clearly reduced. The enhanced turbulence above the IPC strips goes downstream and then increases the momentum transport of the corresponding downstream region, further leading to the delay of the separation. The enhanced turbulent coherent structures above the IPC strips can be observed downstream of the controlled region and extend to the free-shear layer above the ramp, as illustrated in Figure 4b. It can be seen from Figure 5b that there exists a plateau within the separated near-wall region for the baseline case whilst this plateau is lifted up after imposing SADS control. This indicates that the control method adopted in the present study definitely increases the pressure in the recirculation zone and plays a positive role in the recovery of the separated flow.

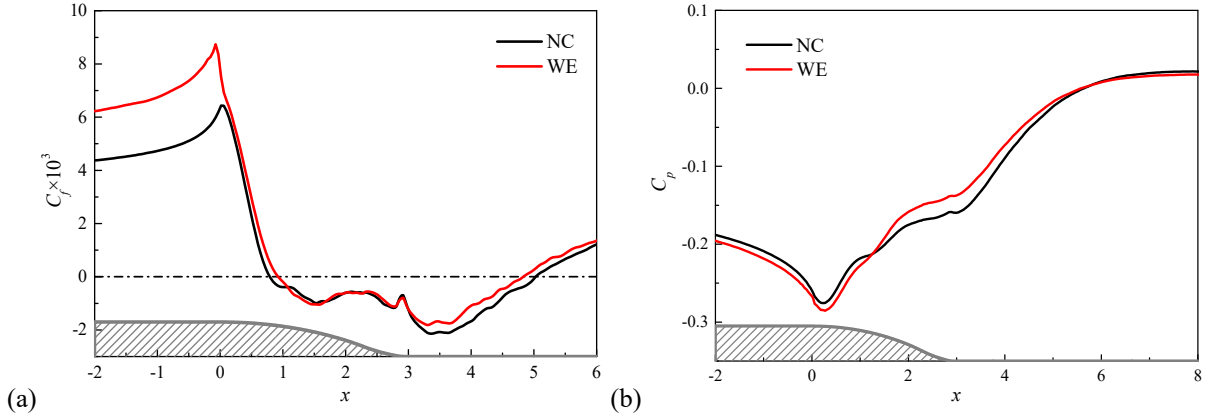


Figure 5: Skin friction coefficient C_f (a) and pressure coefficient C_p (b) based on spanwise- and time-averaging flow field. The grey line at the bottom of the figure and its underneath filled area represent the profile of the geometry adopted in the present study.

The distribution of the skin friction coefficient and the limit streamlines for Cases NC and WE calculated by the time-averaging statistics are plotted in Figure 6. In general, the skin friction coefficient is increased over the IPC strips due to a rise in the local turbulence intensity. It grows to the largest extent at the end of the control area and thus leads to a peak value of the skin friction coefficient obtained in the corresponding position, which is consistent with the results as shown in Figure 5a. Contrastively, the skin friction coefficient is reduced on the OPC strips. Similar spanwise distribution of skin friction coefficient for the controlled cases can be observed in the preparatory work of the turbulent channel flow [8],[9]. As reported by Mejia-Alvarez *et al.* [26], the abrupt wall stress variation would induce transverse turbulent mixing which is the source of a δ -scale secondary flow. Therefore, the spanwise heterogeneities of skin friction generated by SADS control would induce large-scale streamwise structures.

The skin friction lines for Cases NC and WE are plotted to describe the organization of 3-D flows. For Case WE, distinct nodes can be observed right downstream of the IPC strips whereas saddles are observed between neighboring nodes downstream of the OPC strips, as illustrated in Figure 6b. The flow topology of Case WE is clearly reorganized by alternatively distributed OPC and IPC strips. Both of the cases present 3-D structures around the reattachment points. According to Figure 6, 5 attachment nodes can be recognized in Case NC whereas the number of the nodes in the corresponding region are reduced to around 3 in Case WE. Therefore, in the controlled case, the spanwise spacing between neighboring nodes is obviously increased, suggesting the large-scale structure is dominating the flow reattachment. This should be the key for the controlled case to realize the suppression of the flow separation.

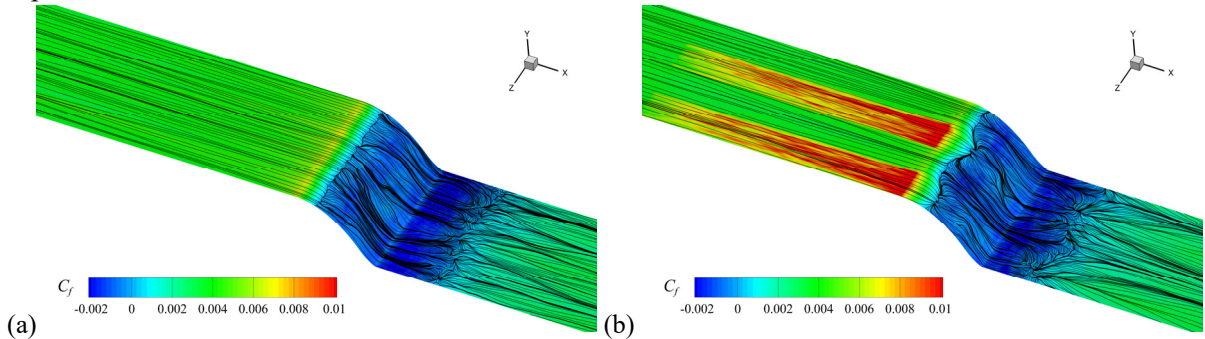


Figure 6: Time-averaging skin friction coefficient and skin friction lines. (a) Case NC; (b) Case WE.

3.3.2 Mean Streamwise Velocity

The profiles of the mean streamwise velocity $\langle \bar{u} \rangle_z$ of Cases NC and WE normalized by the reference velocity are presented in Figure 7 to make an intuitive comparison of the progress on the postponement

of the flow separation and the flow recovery between the baseline case and the controlled case. The zero-streamwise-velocity loci are shown as a dash-dot black line and solid red line for Cases NC and WE, respectively. These zero-streamwise-velocity loci essentially bisect the recirculation zone as mentioned in Bentaleb *et al.* [11]. Compared with Case NC, the SADS control performs a positive role in suppressing flow separation. The velocity profiles in the separation zone are fuller and the height of the recirculation zone is reduced in Case WE. It can be distinctly seen from Figure 7 that the near-wall flow is accelerated under the inflection point of the velocity profile in the recirculation zone after imposing SADS control whereas the velocity in the outer part of the free-shear layer slightly decreases compared with Case NC. This indicates that there exist large-scale structures in the controlled case enhancing the momentum transport between the main flow and the separated flow since the inflection point of the streamwise velocity profile can be regarded as the edge of the separated zone. Thus, the separated flow in the controlled case has a greater potential to realize the flow recovery. It can be also observed from Figure 7 that the inflection points from Case WE move towards the wall compared with those from Case NC, demonstrating that the flow separation is effectively suppressed by SADS control.

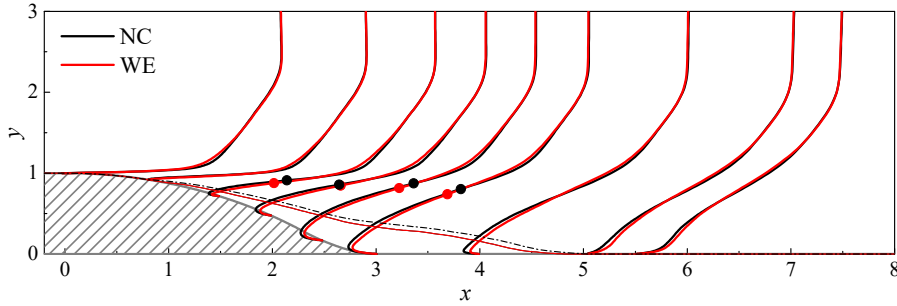


Figure 7: The profiles of the mean streamwise velocity $\langle \bar{u} \rangle_z$ in outer scaling normalized by reference velocity at $x=0.0, 0.8, 1.5, 2.0, 2.5, 3.0, 4.0, 5.0, 5.5$. The zero-streamwise-velocity loci are shown as a dash-dot black line and a solid red line for Cases NC and WE respectively. The black and red solid circles represent the inflection points of the mean streamwise velocity profiles for Cases NC and WE, respectively.

The mean streamwise velocity fields \bar{u} as well as mean velocity vector (\bar{w}, \bar{v}) in the y - z plane at $x=3.0$ of Cases NC and WE are compared in Figure 8 to show the spanwise variation of the mean streamwise velocity in the separated zone reorganized by the SADS control. The zero-streamwise-velocity loci are shown as a dash-dot white line and solid red lines for Cases NC and WE, respectively. The blue and red strips with black borders plotted under the z -coordinate axis represent the corresponding regions downstream of the flat plate surface controlled by OPC and IPC strips, respectively. In order to distinguish the regions genuinely controlled by OPC and IPC strips from those merely influenced by the control method downstream, the latter is named pseudo-OPC and pseudo-IPC respectively hereinafter. It can be seen from Figure 8b that the flow field in the separated zone is reorganized in Case WE compared with the baseline case in Figure 8a. The height of the separation bubble is distinctly reduced above the pseudo-IPC strips along with part of the neighbouring pseudo-OPC strips whereas in the limited regions over the pseudo-OPC strips, the recirculation zone enlarges in the wall-normal direction. A distinct transverse movement of fluid is induced in the controlled case between the neighboring pseudo-OPC and pseudo-IPC strips. Since the penetration depth of the reorganization of the flow field in the recirculation zone for the controlled case can be even beyond the height of the ramp H and the SADS control is only imposed onto the flat plate surface upstream of the backward-facing ramp, we suggest that large-scale structures created in the control area can be sustained in the downstream and interact with the separation bubble and the recovery flow.

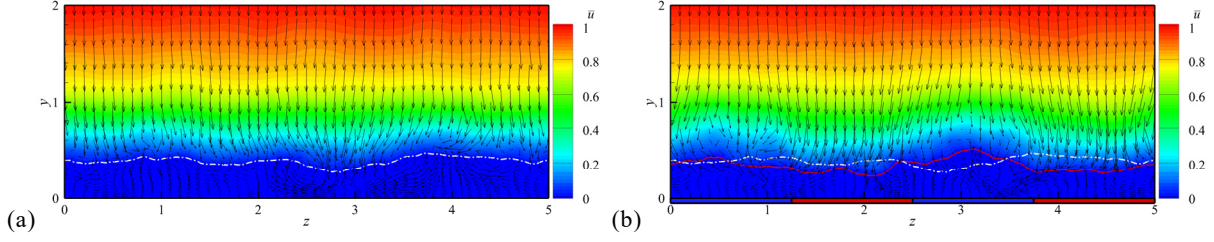


Figure 8: Time-averaging streamwise velocity \bar{u} as well as mean velocity vector (\bar{w}, \bar{v}) of Cases NC (a) and WE (b) at $x=3.0$. The zero-streamwise-velocity loci are shown as a dash-dot white line and solid red lines for Cases NC and WE respectively. The blue and red strips with black borders plotted under the z -coordinate axis represent the corresponding regions downstream of the flat plate surface controlled by OPC and IPC strips, respectively. These regions are named pseudo-OPC and pseudo-IPC respectively in order to distinguish those genuinely controlled by OPC and IPC strips.

3.4 Reynolds Stress

The turbulent kinetic energy (TKE) and Reynolds shear stress (RSS) normalized by the reference velocity are demonstrated in Figure 9, in which TKE and RSS are calculated with time- and z -averaging statistics as,

$$TKE|_{zt} = \frac{1}{2} \langle (u_k - \langle \bar{u}_k \rangle_z) (u_k - \langle \bar{u}_k \rangle_z) \rangle_z (k = 1, 2, 3), \quad (3)$$

and

$$RSS|_{zt} = \langle (u - \langle \bar{u} \rangle_z) (v - \langle \bar{v} \rangle_z) \rangle_z. \quad (4)$$

“ $|_{zt}$ ” represents the fluctuation is calculated by subtracting the z - and time-averaging velocity from the instantaneous one. It can be seen from Figure 9a that before the flow reaches the separation point, the $TKE|_{zt}$ in Case WE is generally increased even up to $y=1.6$ in comparison with the baseline case. RSS in Figure 9b is similar to that of $TKE|_{zt}$. The alike distribution of $TKE|_{zt}$ and $RSS|_{zt}$ for Cases NC and WE can be sustained until $x=1.5$, as illustrated in Figure 9. Higher levels of TKE and RSS have a major contribution to the delay of the flow detachment. Inside the separation bubble, TKE and RSS are still higher for the controlled case at $x=2.0$ due to the history effect. After flowing through the central part of the separated region ($x=3.0$), TKE and RSS of Case WE in the inner part of the boundary layer are gradually becoming smaller than those of Case NC, but in the outer part of the boundary layer, both of TKE and RSS are still higher than those of the non-controlled case, indicating the survive of LSSVs in the free-shear layer.

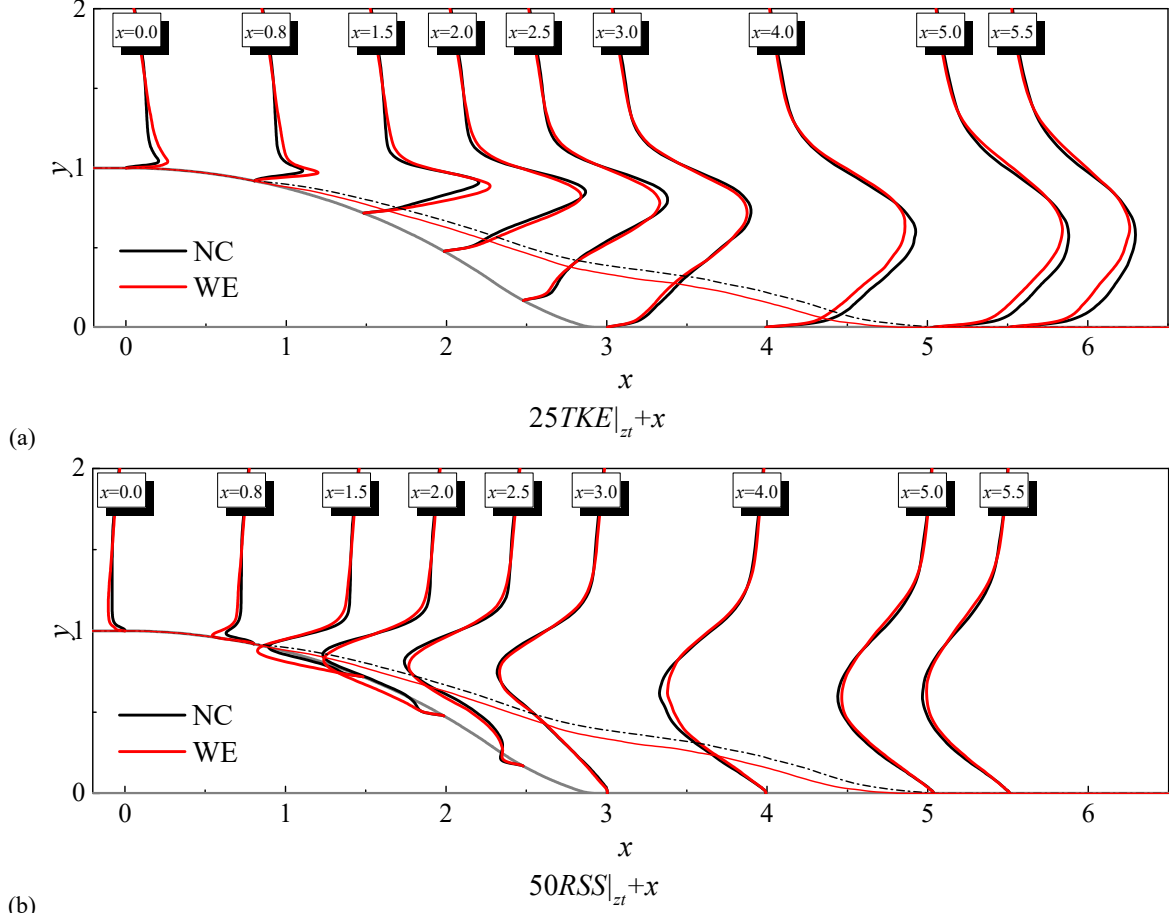


Figure 9: Turbulent kinetic energy (TKE, a) and Reynolds shear stress (RSS, b) calculated by time- and z -averaging statistics of Cases NC and WE at $x=0.0, 0.8, 1.5, 2.0, 2.5, 3.0, 4.0, 5.0, 5.5$. The zero-streamwise-velocity loci are shown as a dash-dot black line and solid thin red for Cases NC and WE respectively. Note that scaling multipliers are used to simply gain an equally clear view of the variations for all quantities.

The distribution of $TKE|_t$ and $RSS|_t$ based on the time-averaging statistics as well as mean velocity vector (\bar{w}, \bar{v}) at $x=3.0$ for the two cases are presented in Figure 10 in order to further study the properties of the LSSV and momentum transport. The definition of $TKE|_t$ and $RSS|_t$ are expressed as $\frac{1}{2}\overline{u'_i u'_i}$ ($i = 1, 2, 3$) and $\overline{u'v'}$ respectively and they are normalized by the square of the reference velocity u_{ref}^2 . “ $|_t$ ” represents the fluctuation is calculated by subtracting the time-averaging velocity from the instantaneous one. For the baseline case, most of the $TKE|_t$ and $RSS|_t$ are confined within the free-shear layer, as shown in Figure 10a and c. It can be seen from Figure 10b and d that, compared with the non-controlled case, the $TKE|_t$ and $RSS|_t$ of Case WE in the free-shear layer present a stronger 3-D effects, indicating they are redistributed by the LSSVs. The clear sweep motions can be observed above the pseudo-IPC strips as illustrated in Figure 10b and d. They bring the high momentum fluid from the free-shear layer into the separation bubble, leading to the high $TKE|_t$ and $RSS|_t$ obtained in the near-wall region. The enhanced turbulent momentum transport results in the decrease of the height of the separation bubble as shown by the solid red lines in Figure 10b and d. It is worth mentioning that the reduction of the height of the separation bubble is not limited in the regions right above the pseudo-IPC strips. On the other hand, the ejection motions take the low momentum fluid from the inner part to the outer region of the separation bubble, enhancing the mixing procedure between the recirculation region and the free-shear layer. Therefore, we suggest the large-scale structures generated by SADS control interact with flow structures in the separation zone and the free-shear layer, leading to the reattachment locations moving forward. The penetration depth of the large-

scale motions displays the same order of the magnitude as the thickness of the turbulent boundary layer.

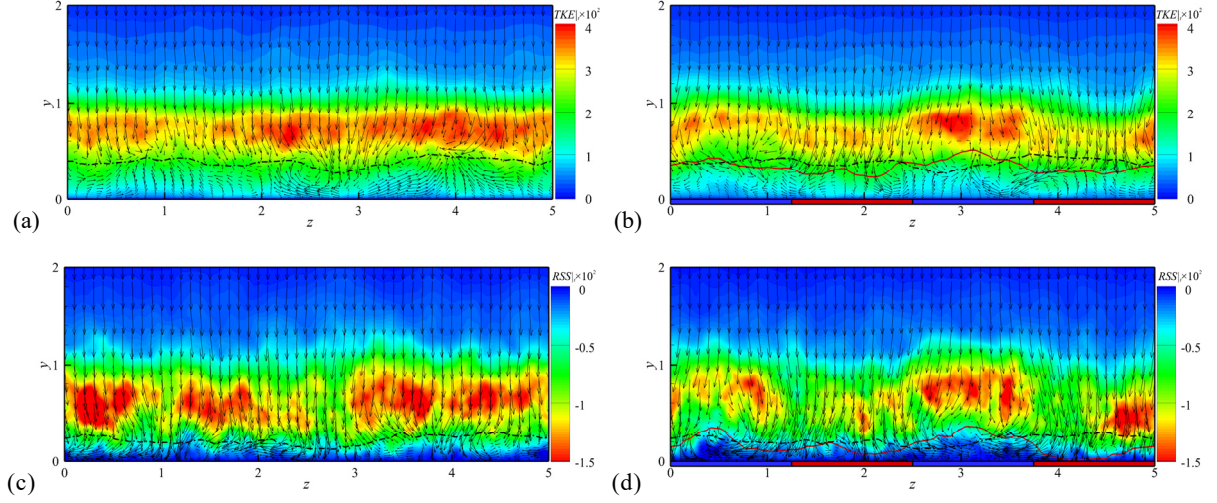


Figure 10: $TKE|_t$ and $RSS|_t$ as well as mean velocity vector (\bar{w}, \bar{v}) of Cases NC (left-hand-side) and WE (right-hand-side) calculated by time-averaging statistics at $x=3.0$. The zero-streamwise-velocity loci are shown as a dash-dot black line and solid red lines for Cases NC and the controlled cases respectively.

4 Conclusion

The Mach=0.2 turbulent boundary layer separation from a backward-facing rounded ramp with SADS control is investigated by ILES. SADS is realized by allocating the spanwise alternatively distributed OPC and IPC strips of wall velocity actuations on the fully developed turbulent boundary layer upstream the ramp. The generation of the large-scale streamwise vortices by such a small-scale control mechanism and their interaction with the downstream separated region are focused. The following conclusions are reached:

- With spanwise alternatively distributed OPC/IPC strips, the distribution of the flow field can be modified in the lateral direction. The turbulent coherent structures are alternatively suppressed and enhanced over OPC and IPC strips for the controlled case. The distribution of the mean skin friction located in the controlled region is reorganized along the spanwise direction and a vertical shear layer is therefore created. The skin friction lines indicate that large-scale structures generated by SADS control exert an influence on the downstream reattachment.
- The analysis presents that the LSSVs are generated by the SADS method. They have an effective interaction with the downstream free-shear layer and then suppress the size of the separated regions. The large-scale structures induced by SADS cause the momentum transport in the wall-normal direction. The sweep motion is towards the IPC strip, bringing the high TKE and RSS from the free-shear layer into the reverse-flow zone, leading to the size of the recirculation region reduced. The ejection side moves away from the OPC strip and an increase in the size of the separation bubble is induced.
- Consequently, the separation point is delayed and reattachment point moves upstream; the size of the separation bubble is obviously reduced. The analysis shows that the delay of the separation point is attributed to the local effect by IPC strips and the improvement of the reattachment location is due to the interaction among the LSSVs, separation zone and free-shear layer.

ACKNOWLEDGMENTS

The project is supported by Department of Research and Advanced Engineering of PSA, UKTC (Grant number EP/L000261/1), Key subjects of National Natural Science Foundation of China (51420105008,

11572025 and 51476004). Weidan Ni was supported by the China Scholarship Council for one-year study at Science and Technology Facilities Council Daresbury Laboratory of United Kingdom. The simulations were conducted on Academic Research Computing High End Resource (ARCHER) supercomputer which is attached to UK National High-Performance Computing Facility.

References

- [1] M. Gad-el-Hak and D. M. Bushnell. Separation control: Review. *J. Fluids Eng.*, 113: 5-30, 1991.
- [2] H. D. Taylor. The elimination of diffuser separation by vortex generators. United Aircraft Corporation Report No R-4012-3, June 1947.
- [3] J. C. Lin. Review of research on low-profile vortex generators to control boundary-layer separation. *Prog. Aerosp. Sci.*, 38: 389-420, 2002.
- [4] H. Babinsky, Y. Li, and C. W. Pitt Ford. Microramp control of supersonic oblique shock-wave/boundary-layer interactions. *AIAA J.*, 47(3): 668-675, 2009.
- [5] B. Nugroho, N. Hutchins and J. P. Monty. Large-scale spanwise periodicity in a turbulent boundary layer induced by highly ordered and directional surface roughness. *Int. J. Heat Fluid Flow*, 41: 90–102, 2013.
- [6] D. Willingham, W. Anderson, K. T. Christensen and J. M. Barros. Turbulent boundary layer flow over transverse aerodynamic roughness transitions: Induced mixing and flow characterization. *Phys. Fluids*, 26: 25–42, 2014.
- [7] C. Vanderwel and B. Ganapathisubramani. Effects of spanwise spacing on large-scale secondary flows in rough-wall turbulent boundary layers. *J. Fluid Mech.*, 774, 2015.
- [8] W. Ni, L. Lu, J. Fang, C. Moulinec and Y. Yao. Large-scale streamwise vortices in turbulent channel flow induced by active wall actuations. *Flow Turbul. Combust.*, 100(3): 651-673, 2017.
- [9] W. Ni, L. Lu, J. Fang, C. Moulinec and Y. Yao. Direct numerical simulation of turbulent channel flow with spanwise alternatively distributed strips control. *Mod. Phys. Lett. B* 32: 1840004, 2018.
- [10] S. Lardeau and M. A. Leschziner, The interaction of round synthetic jets with a turbulent boundary layer separating from a rounded ramp. *J. Fluid Mech.*, 683: 172-211, 2011.
- [11] Y. Bentalb, S. Lardeau and M.A. Leschziner. Large-eddy simulation of turbulent boundary layer separation from a rounded step. *J. Turbul.*, 13: N4, 2012.
- [12] W. Ni, L. Lu C. Le Ribault and J. Fang. Direct numerical simulation of supersonic turbulent boundary layer with spanwise wall oscillation. *Energies*, 9: 154, 2016.
- [13] J. Fang, Y. Yao, Z. Li and L. Lu. Investigation of low-dissipation monotonicity-preserving scheme for direct numerical simulation of compressible turbulent flows. *Comput. Fluids*, 104: 55-72, 2014.
- [14] J. Fang, Y. Yao, A.A. Zheltovodov, Z. Li and L. Lu. Direct numerical simulation of supersonic turbulent flows around a tandem expansion-compression corner. *Phys. Fluids* 27: 125104, 2015.
- [15] J. Fang, Y. Yao, A.A. Zheltovodov and L. Lu. Investigation of three-dimensional shock wave/turbulent boundary- layer interaction initiated by a single fin. *AIAA J.*, 55: 509-523, 2016.
- [16] S. K. Lele. Compact finite difference schemes with spectral-like resolution. *J. Comput. Phys.*, 103:16-42, 1992.
- [17] D.V. Gaitonde and M.R. Visbal. Pade-Type Higher-Order Boundary Filters for the Navier–Stokes Equations. AIAA Paper No. 2103-2112, 2000.
- [18] M. R. Visbal and D. P. Rizzetta. Large-Eddy Simulation on Curvilinear Grids Using Compact Differencing and Filtering Schemes. *J. Fluid Eng.*, 124: 836-847, 2002.
- [19] D. P. Rizzetta, M. R. Visbal and G.A. Blaisdell. A time-implicit high-order compact differencing and filtering scheme for large-eddy simulation. *Int. J. Numer. Meth. Fluids*, 42: 665–693, 2003.
- [20] M. R. Visbal, P. E. Morgan and D. P. Rizzetta. An Implicit LES Approach Based on High-Order Compact Differencing and Filtering Schemes. AIAA Paper 2003-4098, 2003.
- [21] P. Schlatter and R. Örlü. Assessment of direct numerical simulation data of turbulent boundary layers. *J. Fluid Mech.*, 659: 116-126, 2010.
- [22] J. Fang, Y. Yao, A.A. Zheltovodov, Z. Li, and L. Lu. Direct numerical simulation of supersonic turbulent flows around a tandem expansion-compression corner. *Phys. Fluids*, 27: 125104, 2015.
- [23] J. Jiménez, S. Hoyas and M.P. Simens and Y. Mizuno. Turbulent boundary layers and channels at moderate Reynolds numbers. *J. Fluid Mech.*, 657: 335-360, 2010.

- [24]J.C.R. Hunt, A.A. Wray and P. Moin. Eddies, streams, and convergence zones in turbulent flows. Center for Turbulence Research Report CTR-S88, 193-208, 1980.
- [25]J. Fang and L. Lu. Large eddy simulation of compressible turbulent channel flow with active spanwise wall fluctuations. Mod. Phys. Lett. B, 24: 1457-1460, 2010.
- [26]R. Mejia-Alvarez, J. M. Barros and K. T. Christensen. Structural attributes of turbulent flow over a complex topography. Coherent Flow Structures at Earth's Surface, 25-41, 2013.